

RESEARCH

Open Access



# Crack Propagation Analysis of Synthetic vs. Steel vs. Hybrid Fibre-Reinforced Concrete Beams Using Digital Image Correlation Technique

Aniket B. Bhosale and S. Suriya Prakash\*

## Abstract

Improvement in fracture behaviour of fibre-reinforced concrete (FRC) due to the inclusion of various types and combinations of fibres is widely reported. The fracture behaviour of FRC needs to be fully understood for the optimum use of these fibres in structural elements. Fracture behaviours of synthetic fibre-reinforced concrete (SynFRC), hybrid fibre-reinforced concrete (HFRC) and steel fibre-reinforced concrete (SFRC) are investigated in this study using digital image correlation (DIC) technique. This work focuses on improvement in the structural performance of FRC through a comprehensive study of the change in the crack length, crack opening and fracture process zone (FPZ) due to different fibres addition and their combinations. Three distinct fibre dosages of 0.50%, 0.75%, and 1.00%, of macro-polyolefin fibres, hooked end steel fibres and their hybrid combination are regarded as research parameters. Test outcomes indicate that HFRC offers higher post-cracking resistance when compared to SynFRC. SFRC showcases superior fracture performance than that of HFRC and SynFRC. Full-field strain measurements from DIC are used to measure the crack openings at different load levels during the fracture tests. Results of DIC analysis show good agreement with experimental measurements. Continuous monitoring of strain contours using DIC reveals the effective engagement of fibres along the depth at higher dosages for HFRC when compared to that of SynFRC. Also, HFRC had longer cracks than SFRC at a particular load.

**Keywords:** crack length, crack opening, digital image correlation, fibre-reinforced concrete, fracture behaviour, hybrid fibres, macro-synthetic fibres, steel fibres

## 1 Introduction

The fibre-reinforced concrete (FRC) is being used in the construction industry widely across the globe due to its superior mechanical properties, including ductile nature. Some of the previous studies (Alhozaimy et al. 1996; Deng and Li 2007; Rasheed and Prakash, 2015) have concentrated on comprehending the effect of fibre addition on the mechanical properties of concrete. Various types

of fibres, such as artificial (carbon, glass, steel) and natural (leaf, hast, wood) are utilised in construction applications. The main aim of fibre addition to the concrete mix is to improve the fracture performance under flexure and tension loads. Previous studies (Buratti et al. 2011; Caggiano et al. 2012; Li et al. 2018; Lakavath et al. 2019, 2020) have reported a good improvement in post-cracking performance and toughness of concrete due to the addition of steel fibres. Steel fibres are commonly used in concrete construction because of their superior mechanical properties. However, few limitations persist in the usage of steel fibres due to reduced workability of the fresh concrete during casting and their cost. Also, the durability

\*Correspondence: suriyap@ce.iith.ac.in  
Department of Civil Engineering, Indian Institute of Technology  
Hyderabad, Sangareddy 502285, India  
Journal information: ISSN 1976-0485 / eISSN 2234-1315

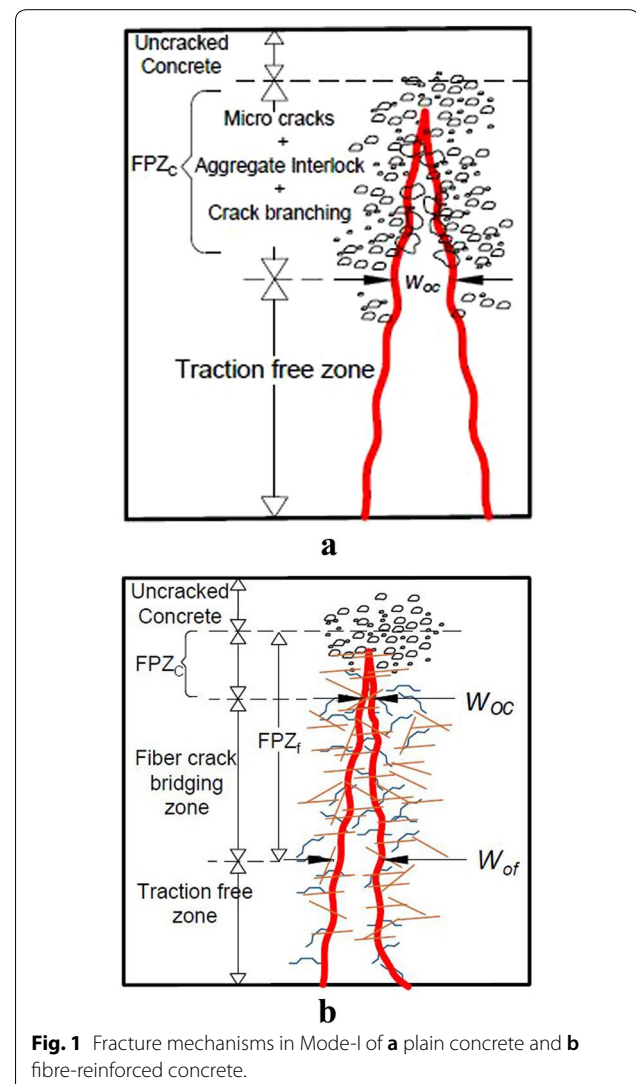
and corrosion of SFRC are enduring problems, which are yet to be fixed. Disadvantages of SFRC have obliged additional investigation towards the full or partial substitution of steel fibres with non-corrosive synthetic fibres.

Synthetic fibres such as polyolefin-based macro-synthetic fibre types can solve the issues of reduced workability of FRC and corrosion without significantly compromising the structural performance. Studies in the past (Buratti et al. 2011; Rasheed and Prakash 2018a, b; Sahoo et al. 2020) showed that the synthetic fibre-reinforced concrete (SynFRC) can impart decent post-cracking behaviour in FRC made with sintered fly ash aggregates. Few studies (Oh et al. 2007; Alberti et al. 2015) in the past have focused on the fracture behaviour of SynFRC and proposed models for fracture response of SynFRC. Though past research has focused on SynFRC, still few limitations exist on the development of design guidelines because the number of fibres at the cracked plane and their orientation across the cracked plane cannot be accurately predicted. Fibre distribution is typically calculated based on the probabilistic approach and its distribution over a plane is assumed to follow the normal distribution (Oh et al. 2007). In SynFRC, the resisting load drops significantly, soon after the peak load and starts to increase at higher displacement (Oh et al. 2007). However, this load drop in SFRC is much lesser when compared to SynFRC. This lower drop in resistance is because of the stiff steel fibres, which are more effective in bridging the crack at lower crack-widths (Buratti et al. 2011). Typically, the residual strengths at specified levels of crack mouth opening displacements (CMOD) are used for evaluating the effectiveness of different fibres. Alberti et al. (2015) compared the residual strengths of SFRC and SynFRC in fracture behaviour tests. They noted the load drops after cracking in SFRC as well as SynFRC and suggested the hybrid combination of these two types of fibres could improve the fracture properties of FRC.

Steel and synthetic fibres can be combined for making a hybrid fibre-reinforced concrete (HFRC). HFRC offers advantages such as retaining the workability and cost reduction (Banthia and Sappakittipakorn 2007; Deng and Li 2007). For considering the hybrid fibre types for structural application, HFRC has to fulfil standard recommendations related to residual strengths (Eurocode 2007), which can be investigated with the help of fracture tests. Thus, comprehending the fracture behaviour of FRC is a sophisticated approach for evaluating the influence of fibres in load resistance. It has been observed that the SynFRC, as well as SFRC, show significant improvement in residual strengths compared to conventional concrete without fibres. Optimisation of various fibre types, combinations, and their dosage is essential for improving the overall performance of HFRC. Thus, understanding the

fracture behaviour of HFRC is crucial to incorporate it into structural design. The fracture behaviour is best understood with the comprehensive research on the fracture process zone (FPZ).

An attempt is to explain the fracture mechanism behind fibre-bridging action and strain redistribution in plain concrete (Control beam) and FRC beams in this study. The mechanisms involved in the fracture of plain concrete and FRC are shown in Fig. 1. Concrete is a heterogeneous material, made of cement, fine and coarse aggregates. Numerous internal cracks in the interfacial zone and pre-existing flaws and micro-cracks in the cement matrix exist in concrete even before any loads are applied. Quasi-brittle materials like concrete exhibit inelastic zone ahead of the crack tip called the fracture process zone (FPZ). FPZ in the plain concrete depends



on the type of aggregate as the aggregate interlock plays a major role in the characteristics of FPZ. Several toughening mechanisms such as micro-cracking, aggregate bridging, crack branching occur in FPZ. Also, the FPZ is responsible for size effect in concrete members. In the case of FRC, FPZ is influenced by the mechanisms in plain concrete and fibre-bridging zone, as shown in Fig. 1. Once the concrete cracks, the stress across the cracked surface will be transferred by the fibres depending on the mechanical properties of fibres and its dosage. This study uses the digital image correlation (DIC) technique (Alam et al. 2014; Dai et al. 2019; Skarżyński and Tejchman 2013; Wu et al. 2011) for understanding the crack opening behaviour. Aggelis et al. (2010) showed that the addition of steel fibres influence the characteristics of FPZ. They employed acoustic emission studies and found the width of FPZ increased marginally, and the length of FPZ increased significantly due to steel fibre addition. However, the effectiveness of different fibres and their combinations in improving the fracture behaviour is not explored well enough.

DIC is a full-field non-destructive measurement technique increasingly used in recent years to understand the behaviour of FRC and to investigate the FPZ (Alam et al. 2014, 2012; Wu et al. 2011). The distant source of measurements allows the DIC technique to be employed for objects exposed to ambient and high-temperature conditions (Rasheed and Prakash 2018b; Srikar et al. 2016; Sutton et al. 2009). Also, the DIC technique is applicable for three-dimensional measurements using two cameras for capturing the images from different angles. DIC can help in the measurement of the length of FPZ (Alam et al. 2014; Wu et al. 2011). Few studies (Reddy and Subramaniam 2017; Gali and Subramaniam 2017; Hu et al. 2011; Robins et al. 2001; Wu et al. 2011; Yang, 2014) have shown that fracture energy is closely related to FPZ size. The relationship between stress and crack opening displacement (COD) in FPZ can be used to describe the softening behaviour of concrete. Though few studies have focused on the use of DIC in the past, their applicability to understanding the behaviour of hybrid FRC is scarce and needs further exploration.

## 2 Research Significance

A critical review of the literature suggests that little work has been reported on the fracture process zone, especially of HFRC using the DIC technique. This study seeks to fill in the knowledge gaps where a combination of steel and synthetic fibres is used to reinforce the concrete matrix. Also, DIC analysis is used as a tool to study the synergistic effect of the fibre combination on the fracture response of the material. The specific objectives of this research are as follows:

**Table 1 Mix design proportions of constituents.**

Constituent	Water	Coarse aggregate	Fine aggregate	Cement
Proportion (kg/m <sup>3</sup> )	144	1062	668	320

**Table 2 Properties of fibres.**

Properties ↓ \ Fibre type →	Polyolefin (synthetic)	Steel
Tensile strength	618 MPa	1000 MPa
Modulus of elasticity	10 GPa	200 GPa
Specific gravity	0.91	7.85
Diameter	0.5 mm	0.6 mm
Length	50 mm	30 mm
Aspect ratio	100	50
Density	910 kg/m <sup>3</sup>	7850 kg/m <sup>3</sup>

1. Characterisation of fracture properties such as fracture energy, average equivalent flexural strength and ductility of SynFRC, SFRC and HFRC materials with different fibre dosages.
2. Investigate the crack lengths and crack openings and their variations over the FPZ as a consequence of different combinations of fibres with the aid of the DIC technique.

## 3 Experimental Programme

### 3.1 Materials

For the casting of FRC specimens, the constituents included synthetic polyolefin fibres, steel fibres, ordinary Portland cement (OPC), potable water, coarse aggregates, and fine aggregates. Table 1 represents the design mix proportions used for casting. The coarse aggregates with nominal diameters of 10 mm and 20 mm were mixed in a ratio of 2:3 by volume. A 53-grade cement (53 MPa) was used as the OPC. Concrete mix design was developed as per IS 10262-2009 (IS 10262: 2009, 2009) with 58 MPa as a target compressive strength. Table 1 showcases the mix design proportions.

For each fibre dosage of same fibre type, three specimens were cast. The dosage amounts were fixed as 0.0%, 0.50%, 0.75% and 1.00% volume fraction ( $V_f$ ). The specimens with 0%  $V_f$  has been termed as control ones. In total, three types of FRCs were cast, viz. SFRC, SynFRC, and HFRC. For obtaining hybrid fibres, both the PO and SF were added with equal volumes. Fibre properties reported by the supplier are given in.

In Table 2 it can be seen that all the three beams in each series were notched and were of dimensions

**Table 3** Cube compressive strength (MPa).

Volume fraction	PO	HB (50% SF + 50% PO)	SF
0.00% (control)	61.63 (1.97)	61.63 (1.97)	61.63 (1.97)
0.50%	58.79 (0.97)	60.06 (1.02)	65.66 (0.40)
0.75%	49.67 (1.40)	61.66 (0.52)	63.09 (1.83)
1.00%	51.77 (0.40)	53.46 (0.40)	65.36 (0.47)

Standard deviations in MPa are given in the parenthesis.

150 mm × 150 mm × 500 mm. Also, cubes of size 150 mm × 150 mm × 150 mm were cast to investigate the compressive strength of FRC. A summary of the compressive strength and coefficient of variation details is represented in Table 3. Each specimen is labelled by the fibre type and fibre dosage it contains. For instance, PO100-1 represents synthetic polyolefin fibre-reinforced concrete specimen having 1.00%  $V_f$  of fibres, where ‘PO’ is a short form for ‘Polyolefin.’ ‘C’ is for ‘control specimens,’ ‘SF’ for ‘Steel fibre’ and ‘HB’ for ‘Hybrid’ specimens. A combination of 50% of steel and 50% of synthetic fibres are used in the hybrid mixture at each fibre dosage. The number at the end in the specimen label designates specimen number in the respective series. The cube test results of the mean compressive strengths and the standard deviations in ‘MPa’ are given in Table 3.

### 3.2 Test Setup and Instrumentation

Notched beams of dimensions 150 mm × 150 mm × 500 mm were used for three-point bending tests. The notch of 5 mm width and 25 mm depth was cut at the mid-span on the side perpendicular to casting face as per the guidelines of EN 14651-2005 (BS EN 14651, 2005). Two roller supports were kept at a clear span of 450 mm. This study focuses on the use of DIC technique to understand the fracture behaviour. Only salient test results are summarised in this paper for the sake of completeness. The vertical displacement at the mid-span of the specimen was measured using a linear variable displacement transducer (LVDT). The crack mouth opening displacement (CMOD) and crack tip opening displacement (CTOD) were measured using clip gauge attached to the mouth of the notch and tip of the notch, respectively. A servo-controlled hydraulic flexure-testing machine (Fig. 2) was used to conduct the fracture test in a displacement-controlled mode. The opening rate of 0.05 mm/min for CMOD was used to control the testing.

### 3.3 Digital Image Correlation Monitoring

A 2-D DIC setup consists of a single camera, in this case, having a 1024 × 768 pixels resolution. All images were

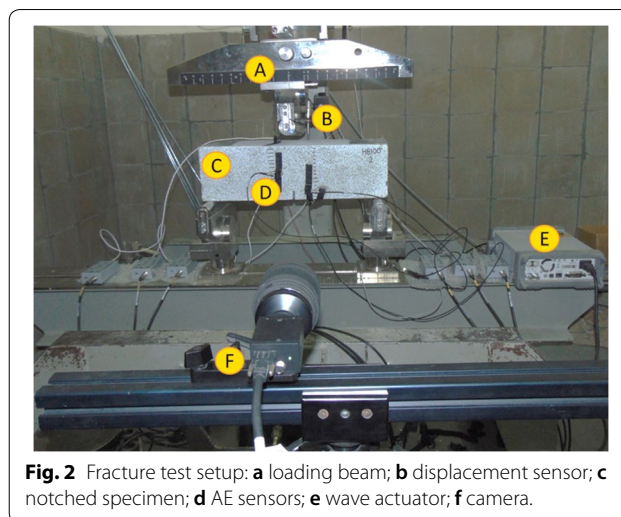


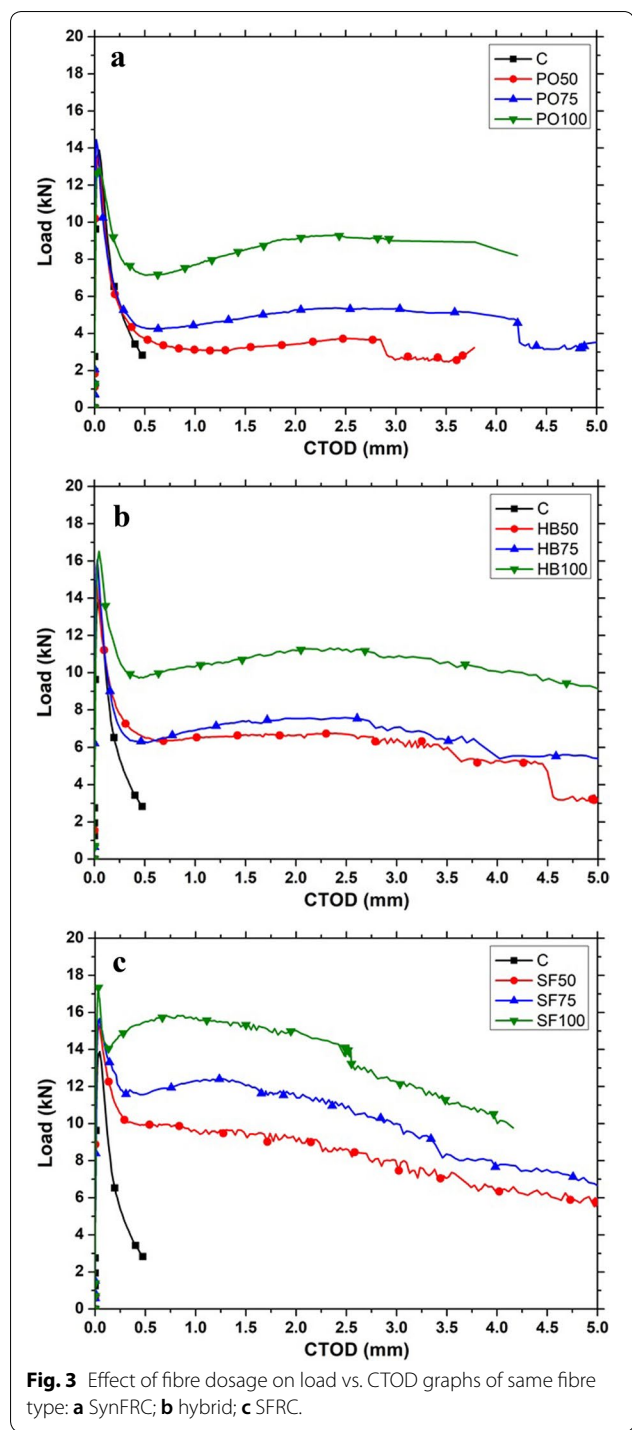
**Fig. 2** Fracture test setup: **a** loading beam; **b** displacement sensor; **c** notched specimen; **d** AE sensors; **e** wave actuator; **f** camera.

captured at a frequency of 2 Hz and stored in a host-computer for post-processing analysis at a later stage. The underlying principle of the DIC analysis is to track the speckles in deformed images with speckles in the reference image within the selected area of interest (AOI). The deformations are measured by finding the distance between the original and deformed coordinates based on the calibration of the image. More details on DIC technique can be found elsewhere (Bhowmik and Ray 2019; Rasheed and Prakash 2018b; Srikar et al. 2016; Sutton et al. 2009; Wu et al. 2011).

## 4 Test Results and Discussion

### 4.1 Flexural Fracture Test

The fracture tests under flexure were conducted to understand the influence of fibres towards load resistance and post-cracking behaviour. Finding the equivalent flexural strength from the fracture behaviour is essential for considering the aid of fibres in structural design. Inspection of the post-cracking behaviour is crucial for acknowledging the effectiveness of fibres in improving the ductile properties of FRC. The load–CTOD performance of all the specimens is vital in this research as, unlike load–CMOD graphs. The load–CTOD curves can directly be compared with the DIC results because the area of interest does not fully extend till the bottom-most layer of the beam. The load–CTOD graphs of all specimens as per the different fibre types and their dosages are shown in Fig. 3a–c. There are three crucial characteristics which outline the behaviour in fracture: the peak load ( $F_L$ ) as per UNI 11039-2:2003 (UNI 11039-2:2003, 2003), the minimum load ( $F_{\min}$ ) immediately after the peak and second maxima ( $F_{\max}$ ), i.e. the peak load following  $F_{\min}$ . Addition of fibres marginally improved the peak load ( $F_L$ )

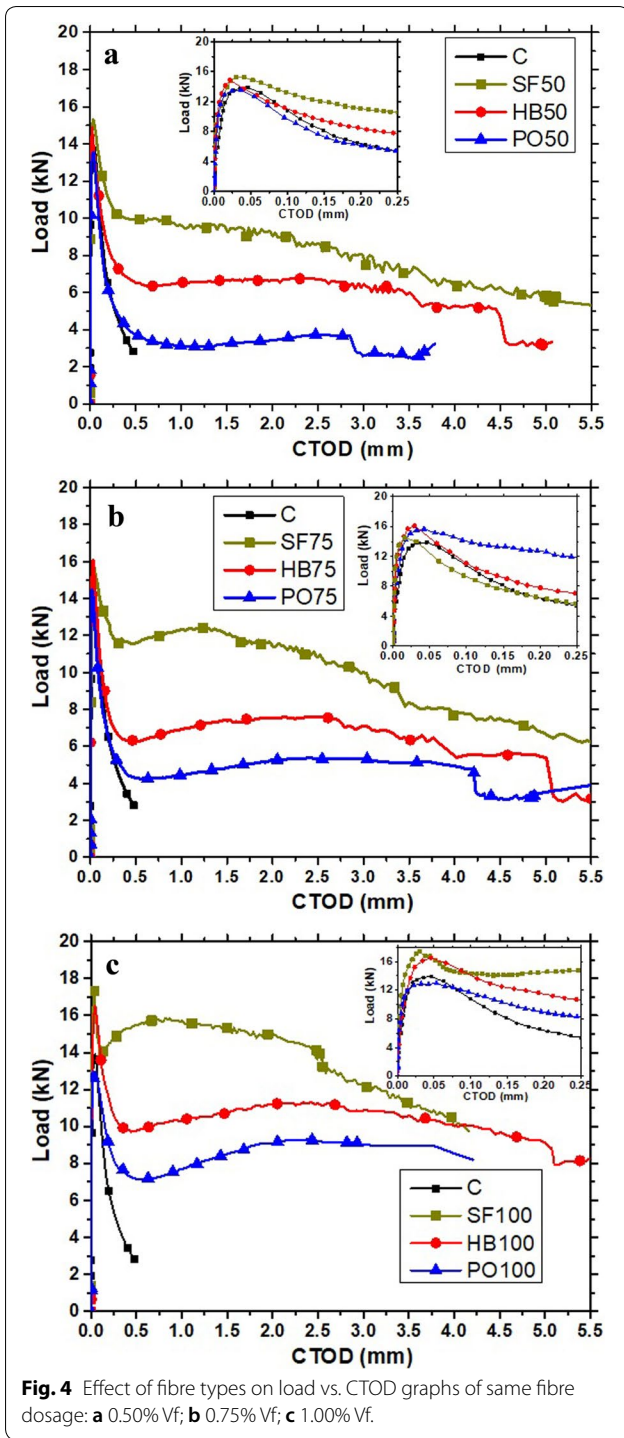


of all the specimens except the SynFRC specimens. The peak load ( $F_L$ ) of SynFRC marginally reduced. The effectiveness of fibres in the crack arresting mechanism at the crack initiation stage depends on the stiffness of the fibres used in the FRC. As a result of lesser stiffness of synthetic fibres, the SynFRC prism does not possess the capability

to produce large stresses in smaller strains; whereas in the case of SFRC prisms, the steel fibres can produce larger stresses as a result of its higher elastic modulus. At the time of peak load, crack initiated in the notch and propagated towards the compression side of the beam. Due to the low elastic stiffness of synthetic fibres, it could not arrest the load drop before its significant stretching. Therefore, the  $F_L$  of SynFRC reduces before re-gaining at larger crack widths. After crack initiation, the load–CTOD curve of the control specimen demonstrates a sudden decay. However, the FRC specimens exhibited significant residual strengths resulting in better post-crack performance and toughness. The continual energy dissipation during the fracture of the specimen to stretch the fibres or to prevail over the bond strength, through the rupture of fibres or fibre pull-out, respectively, results in the enhanced ductility of the FRC specimens. Initially, the resistance after cracking is an outcome of the fibre stretching and subsequently, the combination of fibre pull-out and fibre rupture. The concrete matrix cracking at the peak causes significant loss of stiffness which in turn results in the softening witnessed in all the curves after the first cracking.

In a broader perspective, the FRC specimens showed a similar trend in load–CTOD performance to what was observed in load–CMOD behaviour in earlier work (Bhosale et al. 2019). The load retrieval commencement from  $F_{min}$  is earliest in SFRC specimens, followed by HFRC, then SynFRC (Fig. 4). Also, as volume fraction ( $V_f$ ) of fibres is increased for the same FRC, the load resistance of specimen enhanced significantly (Fig. 3). For all the specimens, with each increment in the fibre dosage, the  $F_{max}$  can be seen improving, along with an increase in the difference between  $F_{max}$  and  $F_{min}$ , whereas, the difference between  $F_{max}$  and  $F_L$  decreased simultaneously.

A hybrid mixture of synthetic and steel fibre reinforcements could improve both the ability of concrete to resist fracture effectively and the toughness. The crack arresting ability of hybrid fibres is shown by the load–CTOD curves in (Figs. 3b, 4). From Fig. 4, it can be seen that the synergistic reinforcing effects of the PO and SF are evident. The mixing of fibres with dissimilar mechanical and geometrical properties results in an improvement in performance at diverse levels. Hybrid fibre addition enhances the strength and stiffness of concrete at different ranges of CTOD. Superior stiffness of SF helps the SFRC specimens to arrest the sudden load drop after the peak. The significant load resistance of SynFRC specimens over high values of CTOD owes to a lengthier bonding length between the concrete matrix and the polyolefin fibres. The HFRC specimens showcased an average behaviour amid that of SynFRC and SFRC specimens. While getting stretched and pulled out from the concrete



matrix, the energy is expended continually by the fibres in FRC, causing improvement in ductility and toughness.

#### 4.2 Equivalent Flexural Strength Results

The procedure for calculation of first crack flexural strengths and equivalent flexural strengths

recommended by UNI 11039-2:2003 (UNI 11039-2:2003, 2003) was used for the analysis of fracture test results. These flexural strengths can be calculated using equations given below:

$$f_{if} = \frac{1.5(F_L)L}{b(d_{lig})^2}, \tag{1}$$

$$f_{eq(0-0.6)} = \frac{1.5(U_1)L}{0.6b(d_{lig})^2}, \tag{2}$$

$$f_{eq(0.6-3)} = \frac{1.5(U_2)L}{2.4b(d_{lig})^2}, \tag{3}$$

where  $f_{if}$ =first crack flexural strength;  $f_{eq(0-0.6)}$  and  $f_{eq(0.6-3)}$ =equivalent flexural strengths;  $F_L$ =peak load (N);  $L$ =clear span (mm);  $b$ =width of beam (mm);  $d_{lig}$ =depth of ligament (total depth – notch depth) (mm).  $U_1$  and  $U_2$  are the toughness energies representing contributions of concrete and fibres, respectively, in the energy absorption process. These are calculated by using the area under load–CTOD response as given by Eqs. (4) and (5) as per UNI 11039-2 (UNI 11039-2:2003, 2003). These post-cracking equivalent flexural strength values mentioned above are important for serviceability limit state and ultimate limit state, respectively.

$$U_1 = \int_0^{0.6} F(CTOD).d(CTOD) \tag{4}$$

$$U_2 = \int_{0.6}^3 F(CTOD).d(CTOD) \tag{5}$$

Using the above values, ductility indexes can be calculated as:

$$D_0 = \frac{f_{eq(0-0.6)}}{f_{if}}, \tag{6}$$

$$D_1 = \frac{f_{eq(0.6-3)}}{f_{eq(0-0.6)}}. \tag{7}$$

As per Eqs. (1) to (7), the equivalent flexural strengths and ductility indexes are calculated at the serviceability and ultimate limit state and are summarised in Table 4 for different fibre types with varying fibre volume fractions. These ductility indexes have been evaluated as per the standard UNI 11039-2 (UNI 11039-2:2003, 2003). These indices are not analogous to the ductility generally calculated based on the ratio of ultimate deformation to yield deformation. These ductility indexes used in this study represent how much of reserve strength is available

**Table 4 Average equivalent flexural strength calculation for all specimens.**

Specimen	$F_L$ (kN)	$f_{ff}$ (N/mm <sup>2</sup> )	$f_{\text{Equation (0-0.6)}}$ (N/mm <sup>2</sup> )	$f_{\text{Equation (0.6-3)}}$ (N/mm <sup>2</sup> )	$D_0 = (f_{\text{Equation (0-0.6)}}/f_{ff})$	$D_1 = (f_{\text{Equation (0.6-3)}}/f_{\text{Equation (0-0.6)}})$
Control	13.911	4.01	1.57	–	0.39	–
PO50	13.596	3.92	1.76	0.97	0.45	0.55
PO75	14.550	4.19	1.86	1.43	0.44	0.77
PO100	12.967	3.73	2.53	2.48	0.68	0.98
HB50	14.886	4.29	2.41	1.90	0.56	0.79
HB75	16.083	4.63	2.35	2.09	0.51	0.89
HB100	16.531	4.76	3.23	3.12	0.68	0.97
SF50	15.325	4.41	3.19	2.63	0.72	0.82
SF75	17.115	4.93	3.58	3.32	0.73	0.93
SF100	17.345	5.00	4.34	4.23	0.87	0.98

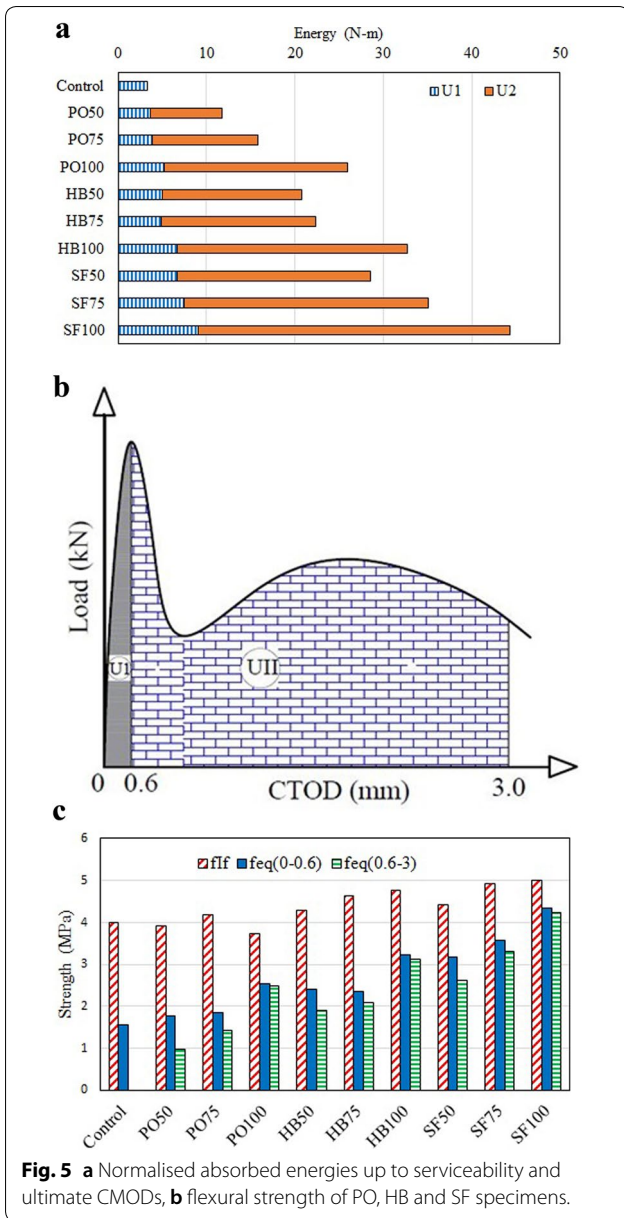
at that limit state relative to the prior strength because of continual damage.

Figure 5a shows the energy contributions in the fracture of the beam until the serviceability limit state ( $U_1$ ) and at the ultimate limit state ( $U_2$ ). The addition of these two energies gives the total toughness energy absorbed over the fracture test, as shown in Fig. 5a. The total toughness energy increases with the increase in  $V_f$  for all the fibre types. Also, it shows that more energy is required to fracture a beam reinforced with stiffer fibres like the steel as compared with the polyolefin fibres of the same  $V_f$ . Much of the energy absorption comes from the  $U_2$  contribution in all of the beams. From Fig. 5a, it is seen that the energy absorbed in the second phase of fracture ( $U_2$ ) improves with a higher rate than that of the energy absorbed in the first phase of fracture ( $U_1$ ) as we go on adding the fibres in the concrete. The absorbed energy is calculated according to UNI 11039-2. In energy calculations, the first phase ( $U_1$ ) covers the CTOD range from 0 to 0.6 mm. Similarly, the second phase ( $U_2$ ) covers the range of 0.6 to 3 mm as shown in Fig. 5b. It has been observed that the addition of fibres in the concrete matrix improves the fracture response of the FRC mainly after the crack formation. With the increase in fibre dosage, the second peak load increases significantly due to better fibre-bridging action as compared to the improvement in the first peak load in the first phase of fracture. Thus, the energy absorbed in the second phase of fracture was significant than that of the energy absorbed in the first phase of fracture. This strengthens the pre-established fact that the addition of fibres majorly improves the post-cracking performance of the concrete significantly owing to the increased resistance against crack opening by the fibre-bridging action.

These larger improvements in  $U_2$  values result in higher increments in flexural strengths ( $f_{eq(0-0.6)}$ ) causing the  $D_1$

ductility indexes to improve with an increase in  $V_f$ . Figure 5c depicts the specimen-wise variation in the flexural strengths of the FRC beams. The results portray that SFRCs have the highest flexural strengths and ductility indexes. Similarly, HFRCs show the median flexural strengths, and ductility indexes between the steel and synthetic fibre-reinforced specimens. In addition to this, an observation can be made from Fig. 5(c) that the gap between the last two flexural strengths closes rapidly in the SynFRC specimens with an increase in  $V_f$  compared to other FRCs. This makes the SynFRC among all types of FRCs to exhibit the highest improvement rate for  $D_1$ , i.e. ductility index corresponding to the ultimate limit state, with an increase in  $V_f$ . That means for the same increment in  $V_f$  the SynFRC showcases the highest increment in  $D_1$ , and HFRC shows a better increment in  $D_1$  than SFRC for a higher dosage. The increment in  $D_1$  endorses that the best performing range of SynFRC lies in higher CTOD values.

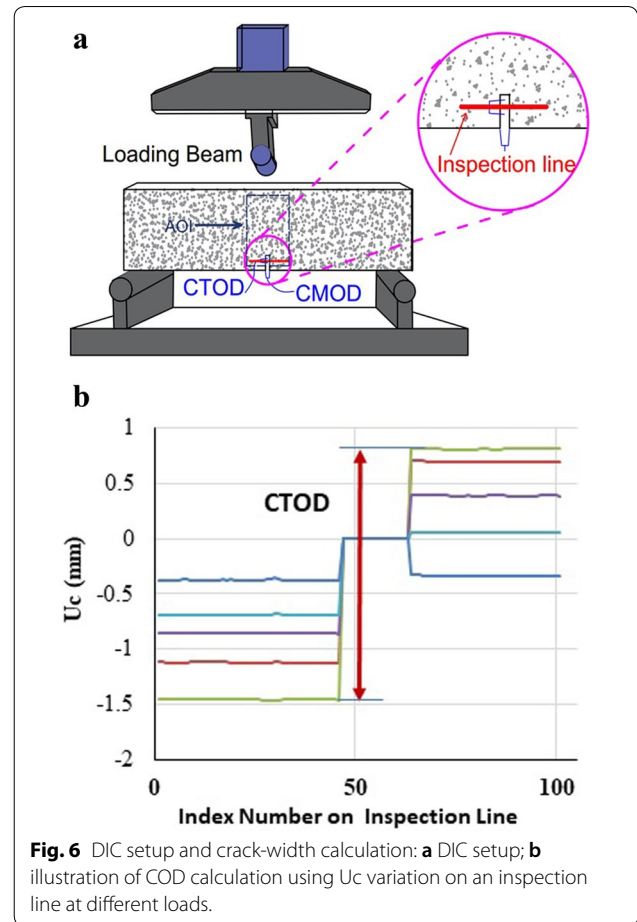
Due to an increase in the fibre dosage, the ductility index increased at both the serviceability and ultimate limit state. SFRC specimens had higher ductility indexes at both the ultimate and serviceability limit states. At the ultimate limit, higher fibre dosage specimens of hybrid and synthetic fibres had nearly the same ductility indexes as that of steel fibres (Table 4). The ductility index ( $D_1$ ) is the ratio of average equivalent flexural strength of different CTOD ranges ( $D_1 = (f_{eq(0.6-3)}/f_{eq(0-0.6)})$ ). At the higher fibre dosages of the specimen, the respective increment due to equivalent flexural strength is similar, resulting in the same values of the ductility index at higher fibre dosages. SFRC had higher equivalent flexural strength when compared to other FRCs. The ductility index is the measurement of improvement in the equivalent flexural strengths of the same specimen over different ranges of CTOD. It does not give the value of equivalent strength



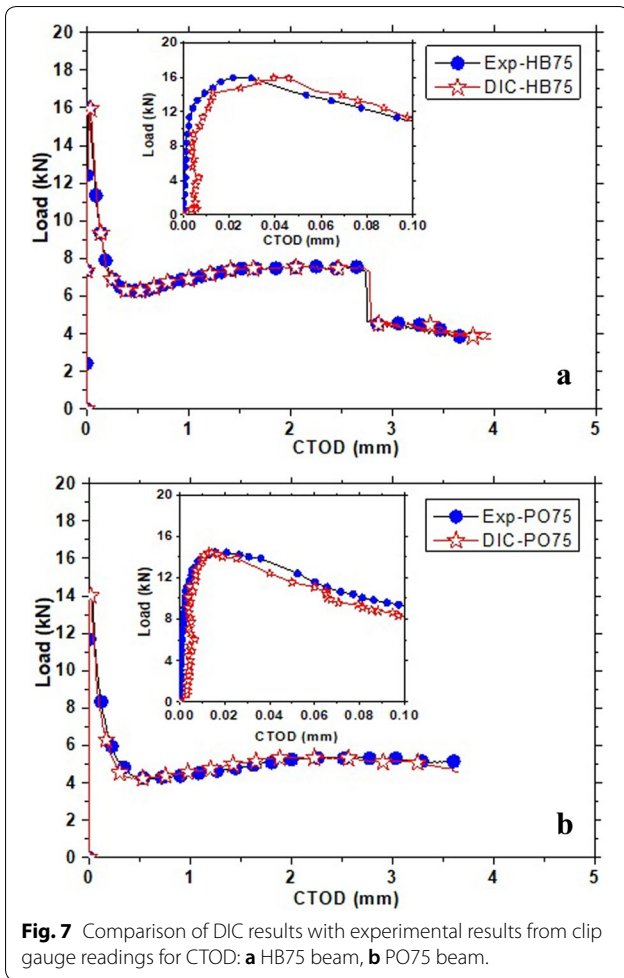
but the ratio of equivalent strengths. The results show that synthetic and hybrid fibres are more effective at higher crack widths corresponding to the ultimate state.

### 4.3 DIC Analysis Results and Discussion

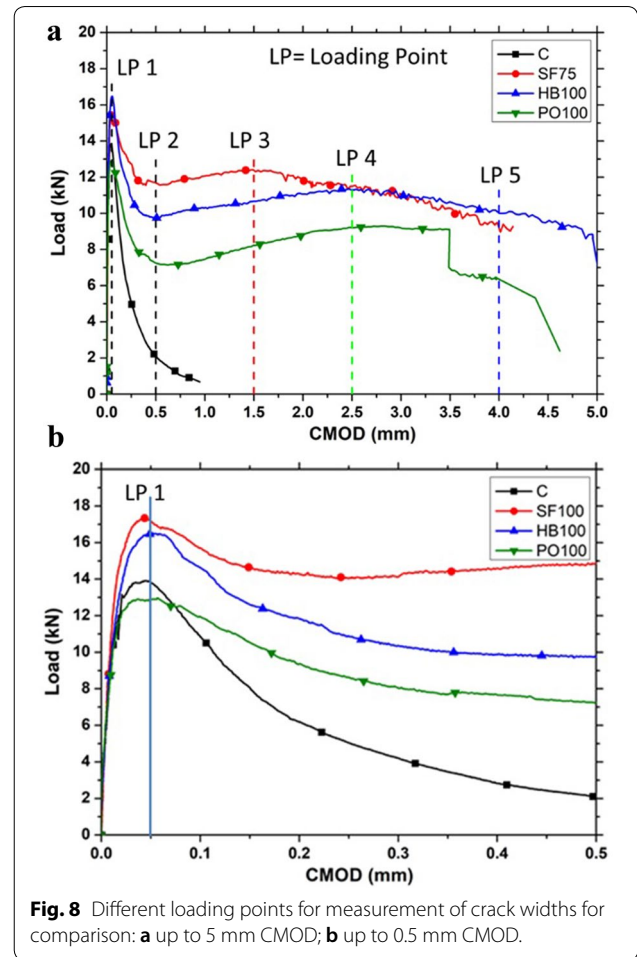
DIC technique was used to measure full-field strain and displacement of prism specimens in the fracture test. Figure 6a shows the DIC setup used during fracture test. The digital images captured using the DIC camera were analysed using Vic-2D™ 2009 software. The post-processing of captured images was carried out using the same software for extracting the DIC-based results.



The horizontal displacements ( $U_c$ ) of the notch can be extracted at required depth on the surface of the specimen by line inspection gauge. Figure 6b illustrates the extracted horizontal displacement ( $U_c$ ) variation at the level of crack tip opening displacement (CTOD) against index points on the inspection line. The line drawn at the CTOD clip gauge level on a digital image is divided into 101 index points, to extract 101 readings from the line inspection gauge. In Fig. 6b, in the middle part, the values of displacement are zero because those are the points overlapping with the notch opening. At the notch location, the absence of correlation results in null displacements. The difference in horizontal displacements on either side of notch gives the value of CTOD from DIC analysis. The post-processed images were used to measure CTOD values. The load–CTOD curves from DIC and experimental clip gauge measurements are compared in Fig. 7. The quality of speckling is confirmed by greyscale patterns and light source in the focused area. The even distribution of speckles was ensured with different random sizes making each



subset unique which in turn makes it easier to correlate the images in the software. After that, the images were captured to identify the crack pattern and its propagation throughout the testing. However, the pattern of speckling remains unique for each specimen. Thus, the correlation coefficient cannot be similar for all the specimens. Though there is variation in speckling patterns and correlation coefficients, the first image of each specimen is used as a reference image for measurement of crack lengths and for correlating all the images after deformation of the same specimen. The accuracy of the crack formation is ensured based on previous literature and calibrations with load–CTOD response comparison with theoretically obtained CTOD response. The accuracy of DIC results depends on the size of the speckles and subset size. Based on previous studies by (Crammond et al. 2013; Lecomptea et al. 2005; Park et al. 2017; Reu, 2015) the subset size and speckle on prism specimens were incorporated.



#### 4.4 Load Versus CTOD Curves

From Fig. 7, it can be confirmed that all the results from DIC are consistent with the fracture test results. The COD values calculated from DIC results are very close to the CTOD values measured using clip gauge in the fracture test. Thus, comparison proved that the DIC results are reliable and accurate for further detailed analysis. A general trend was identified from the previous results to understand the changes in horizontal strain ( $\epsilon_{xx}$ ) contours throughout the tests. Five such loading points were selected, as shown in Fig. 8. Loading point 1 (LP1) corresponds to CMOD value 0.05 mm, which is close to the peak load ( $F_l$ ). LP2 corresponds to 0.5 mm CMOD attributing to sudden drop ( $F_{min}$ ) after cracking. Acknowledging the importance of second peak post-cracking ( $F_{max}$ ), LP3, and LP4 limits were set at 1.5 mm and 2.5 mm CMOD, respectively. The last loading point LP5 corresponds to 4 mm CMOD representing the ultimate state.

### 4.5 Comparison of Strain Variations at Different Load Points

With the DIC analysis of images at 0.05, 0.5, 1.5, 2 and 4 mm CMOD values, strain contours of  $\epsilon_{xx}$  over an area of interest (AOI) chosen are shown in Figs. 9, 10, 11 and 12. Figure 11 shows the crack kinematics concerning the steel fibre dosage. Up to the peak (0.05 mm CMOD), the SFRCs and the controls specimens show very little difference and maximum strains are located near the notch tip. With the increase in applied loads, the maximum strain contours shifted to the top region for lower fibre dosages. The control specimen failed at about 1 mm CMOD. For C and SF100 specimens, the DIC correlation broke down at 1 mm. As a result, DIC results are not available for these specimens beyond LP3. Higher fibre dosages show an effective crack arresting as indicated by the presence of continuous maximum strain contours spread along the depth. Figure 9 shows a similar trend for synthetic fibre dosage but with a slightly discontinuous presence of maximum strain contours along the depth. Figure 10 shows DIC analysed images of HFRC concerning increasing CMOD values for different dosages of fibres. Effective fibre engagement is observed at small CMOD values for steel fibres and a higher CMOD value for synthetic fibres. The synergistic effect from the steel fibres and synthetic fibres was obtained for hybrid fibres resulting in effective

engagement of cracks at different levels of CMOD values. It can also be inferred from these contours that the horizontal strain increases from LP1 to LP2 with maximum strain at the tip of the notch and minimum at the top face. With further increase in the CMOD, the horizontal strain levels along the depth increased. The strain may drop down to zero at locations when there is a fibre pull-out or at the location where the fibres were absent for bridging the crack. This strain reduction phenomenon can be observed clearly in FRCs with low  $V_f$  values at loading points corresponding to higher CMOD. However, the strain reduction zone shrunk with an increase in  $V_f$  and the strain distribution increased along the depth of the beam. This is due to more number of fibres available at the cracked surface for bridging the crack. The role of fibres bridging across the crack is one of the reasons for the higher energy absorption of fibre-reinforced specimens before it ruptures.

For comparison, graphs of load–CMOD with varying fibre dosage for each fibre type are represented in Figs. 9, 10, 11 and Fig. 12. A sample comparison of peak load ( $F_L$ ), stiffness and immediate drop after cracking of matrix is plotted in load–CMOD graphs in Fig. 12. This graph mainly concerns with the small CMOD values ranging from 0 mm to 0.5 mm to observe the stiffnesses in the pre-cracked zone. It can be inferred from these

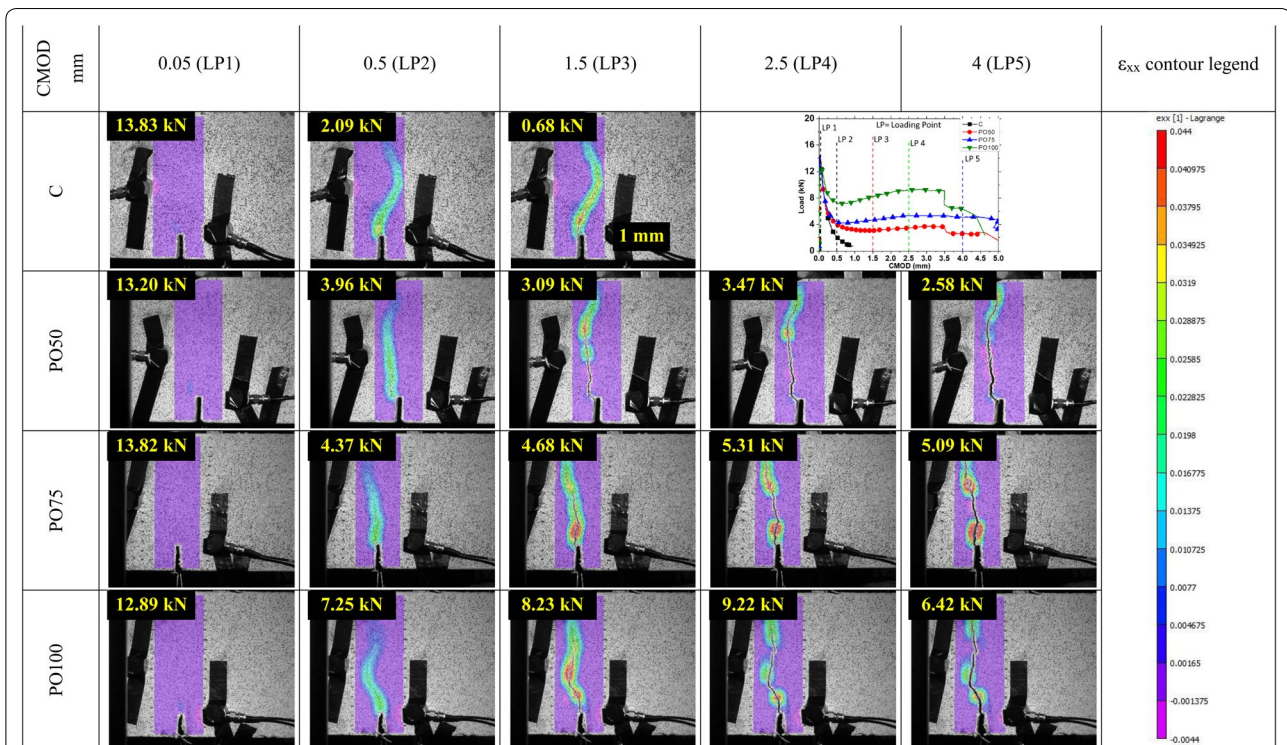


**Fig. 9** Comparison of strains of SynFRC with different fibre dosages at considered CMODs.

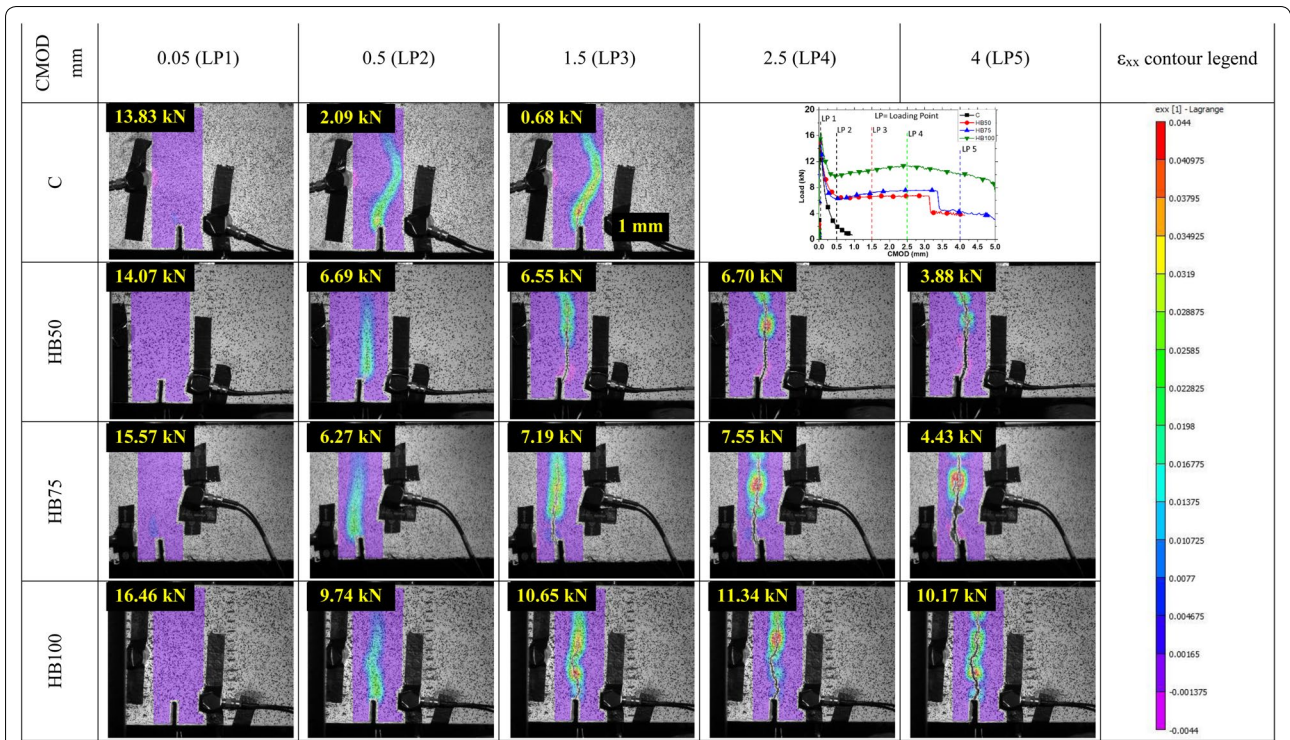


**Fig. 10** Comparison of strains of HFRC with different fibre dosages at considered CMODs.

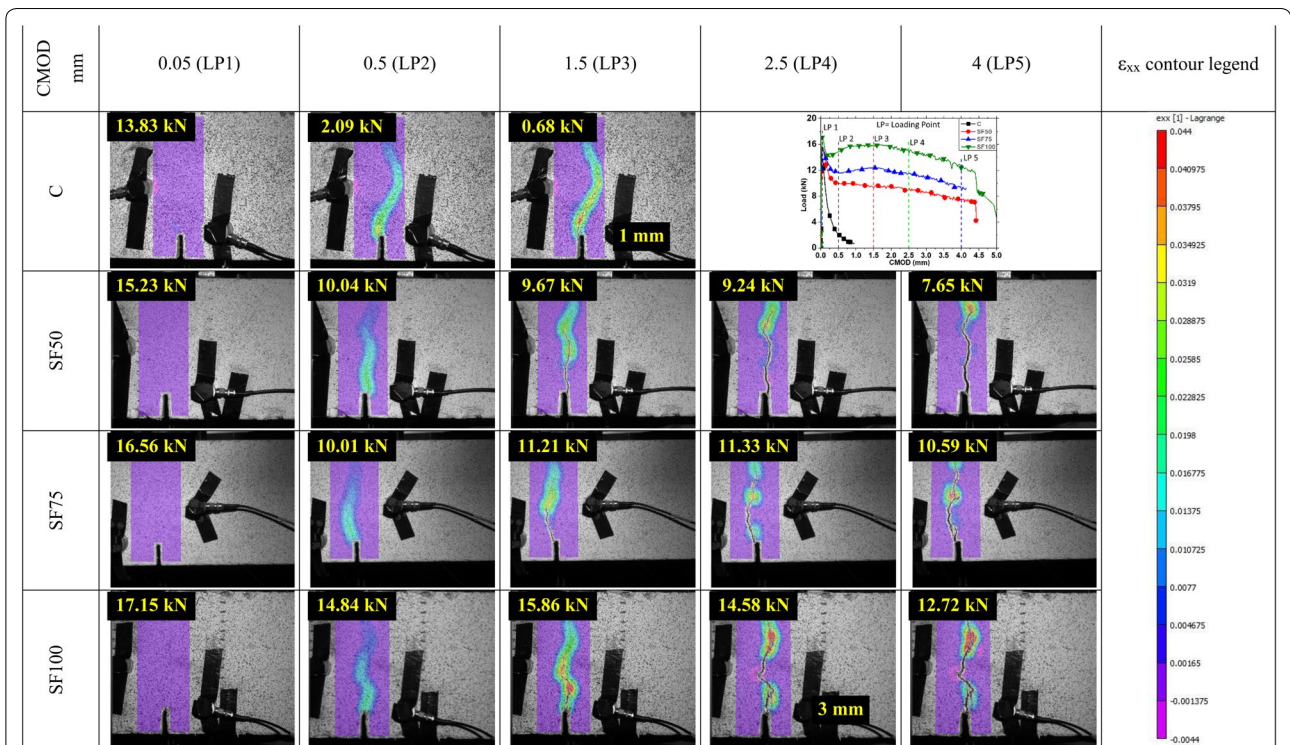
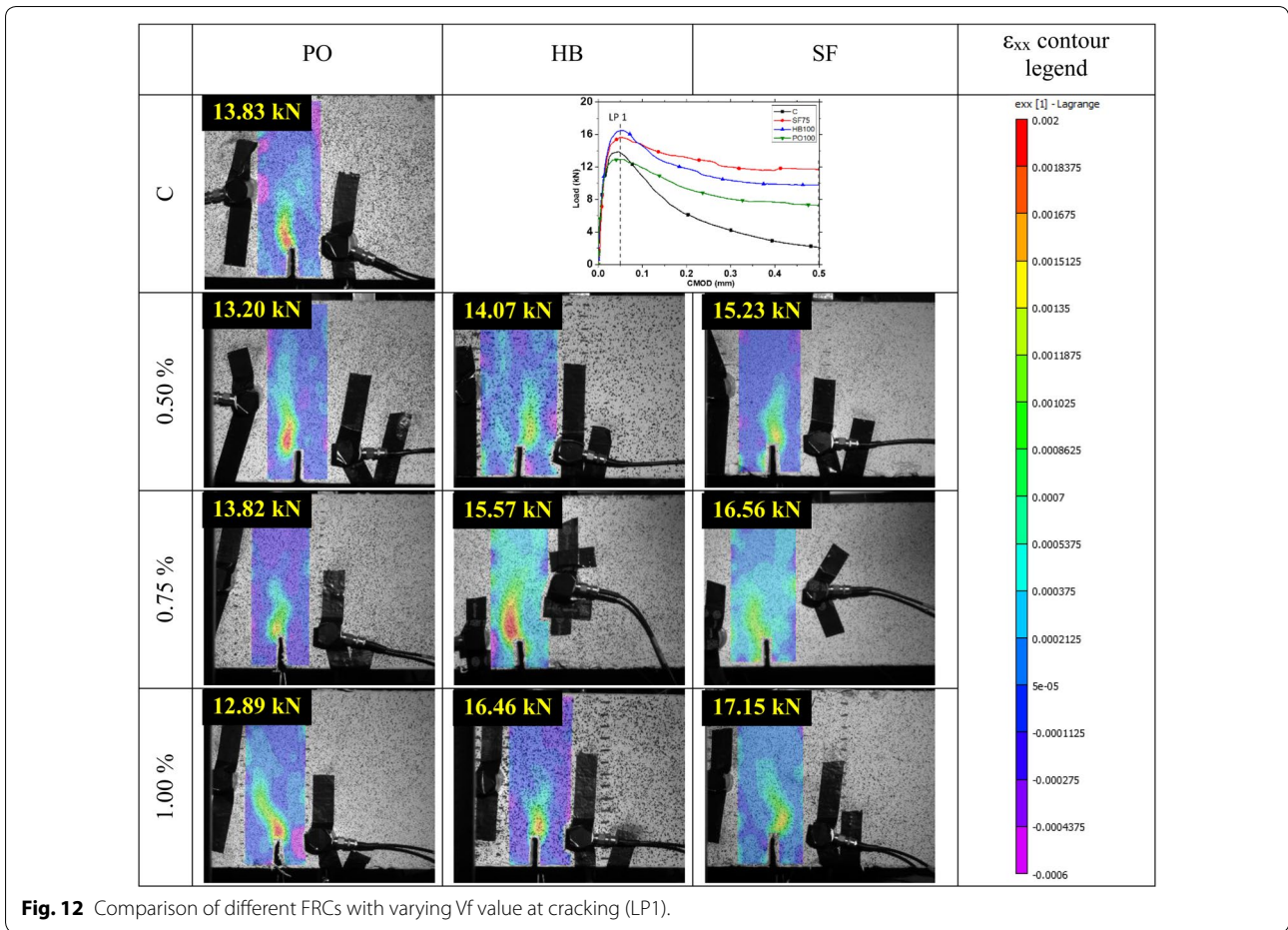


**Fig. 11** Comparison of strains of SFRC with different fibre dosages at considered CMODs.



figures that the load-resisting capacities of different fibre types lie in different ranges after cracking. The resistance range at 0.5 mm CMOD for SynFRC is from 4 kN to 7 kN (Fig. 9), whereas, it ranges from 6 kN to 10 kN for HFRC (Fig. 10) and from 10 kN to 15 kN for SFRC (Fig. 11). This showcases how hybridisation of two different types of fibres helps at service limit state. These graphs confirm that peak loads tend to increase with  $V_f$  except for SynFRC.

Due to the small scale of strain contours from Figs. 9, 10, and 11, at LP1 (near cracking load), the strains are not comparable with that of other load points. The strain values at LP1 can be seen to fall below 0.00165. Therefore, to understand crack initiation behaviour, a separate comparison of strain contours ( $\epsilon_{xx}$ ) at LP1 is represented in Fig. 12 with the smaller scale of strains. The observation of strains at cracking indicates the strain localisation around the tip of the notch. Due to strain localisation, the crack initiation and propagation started from the tip of the notch and gradually moved to the top of the section. The strain contours indicated that the horizontal strain ( $\epsilon_{xx}$ ) contour was distributed and spread more in the

fracture process zone (FPZ) of SFRC and had lower peak strains than SynFRC and HFRC.

#### 4.6 Crack Length and Crack Opening Displacement

A MATLAB program was developed to plot the coefficient of correlation and horizontal displacement ( $U_c$ ) over the chosen area of interest (AOI) on the surface of the beam. The data extracted from the DIC analysis were used as the input to the MATLAB program. In particular, the variations of the coefficient of correlation and  $U_c$  are plotted for better visualisation of the crack opening along the length and across the depth over the chosen AOI. Figure 13 represents a sample plot of the above information for SynFRC (PO50 specimen) at LP5 corresponding to a CMOD of 4 mm. The variation of the coefficient of correlation is important for understanding the length of the crack propagation above the notch. The crack opening results in overlapping of subsets at a crack location due to physical opening at that location. This overlapping causes the loss of correlation relating to those subsets. Thus, a significant difference is observed in the values of the coefficient of correlation over the crack opening and

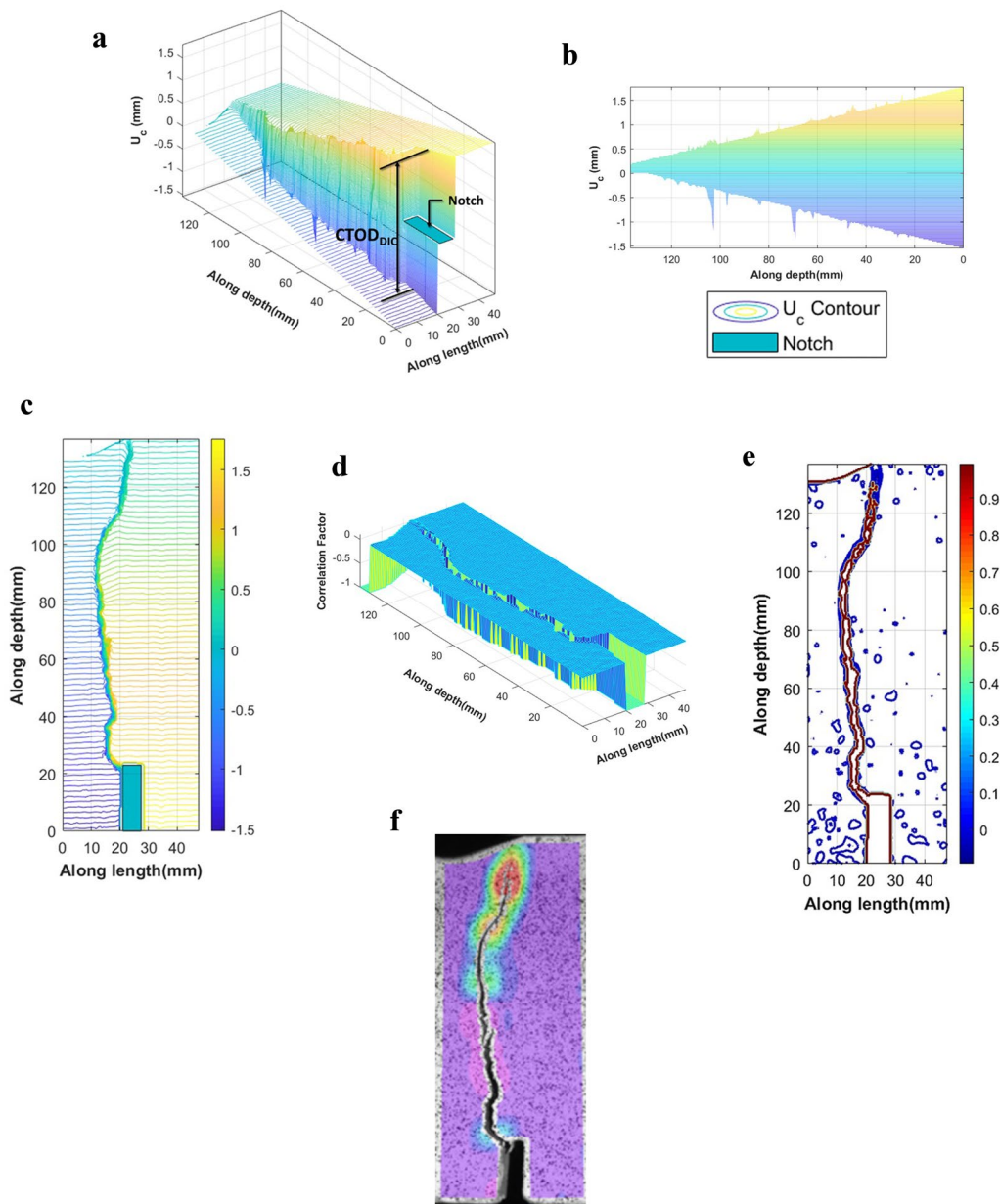


**Fig. 13** Contours of correlation coefficient and visualisation of the crack opening of PO50 specimen at LP5, 4 mm CMOD: **a** 3D visualisation of the crack opening using contour of  $U_C$  over AOI; **b** variation of COD along the depth (side view of 3D contour); **c** distribution of  $U_C$  over AOI (top view of 3D contour); **d** coefficient of correlation over AOI showing physical opening; **e** the contour of the coefficient of correlation over AOI; **f** actual image of AOI in the specimen with  $\epsilon_{xx}$  contour.

away from the crack opening. This method is used for identifying the location of the crack tip and length of the crack.

Figure 13 shows the distribution of the  $U_C$  and coefficient of correlation or correlation factor over the area of interest (AOI) of PO50 specimen at LP5. For this purpose, grid data were extracted at an interval of 5 pixels in both horizontal and vertical directions from DIC analysis.

Figure 13a–c depicts the variation in  $U_C$  in 3D contour and from different views. Figure 13 enables better visualisation of the crack-width measurement using DIC and the variation of the crack width throughout the depth of the beam. Figure 13a also showcases the location of clip gauge for CTOD measurement along the position of the notch in the beam. The distribution of crack widths at all depths can be observed. The slopes of the contour of ' $U_C$ '

in a longitudinal direction away from the crack were very shallow and approximately equal on either side. The steep slope in the contour of ‘ $U_C$ ’ above notch was because of the crack initiation and its propagation from the notch.

In Fig. 13c, the shift in contour shows negative values on the left side of the crack and positive values on the right side. The difference in signs indicates that both sides were moving away horizontally, resulting in the opening up of the crack. This crack opening can be measured, as shown in the side view (Fig. 13b) of this 3D contour. Also, Fig. 13 shows the localisation of displacement contours takes place near the crack. All the contour lines travel perpendicular to the crack propagation away from the crack. Contour lines become parallel to crack propagation near the crack and are stacked very close to each other (dense). This contour pattern indicates that sharp displacement gradient exists near the crack confirming strain localisation around the crack. The strain localisation enabled the crack to emanate from the notch and further propagate upwards.

The physical opening in the crack can cause complete loss of correlation. Presence of cracks causes a significant difference between the coefficient of correlation over the crack opening than the average value away from the crack location. This difference in the coefficient of correlation allows identifying the physical opening of the crack and understand the propagation of the crack. Figure 13d and e represents the contour of the coefficient of correlation over the area of interest (AOI). It clearly shows the physical opening over the notch. The contour with brown colour in Fig. 13e depicts the boundaries of crack opening on the surface of the specimen. These crack propagations and physical openings from all contours are compared with the tested specimen in Fig. 13 at the same load level. Thus, the close agreement of the DIC predictions and experimental measurement proves the capability of DIC in the accurate detection of crack initiation and propagation.

The crack tip can be identified using values of coefficient of correlation over the area of interest (AOI) and by finding out the topmost point exceeding the threshold value of correlation. The threshold value of correlation is the average value of the coefficient of correlation in the region away from the crack location in the AOI. The illustration of identification of crack tip and measurement of crack length from the tip of the notch is represented in Fig. 14, along with the crack length versus CMOD response. The crack length versus CMOD response was of FRC specimens was similar to that of control specimens without fibres. At low CMOD values, the crack rapidly advanced to about 100 mm, i.e. 80% of the depth of the specimen above the notch. A rapid upward movement in the location of the zero-crack opening

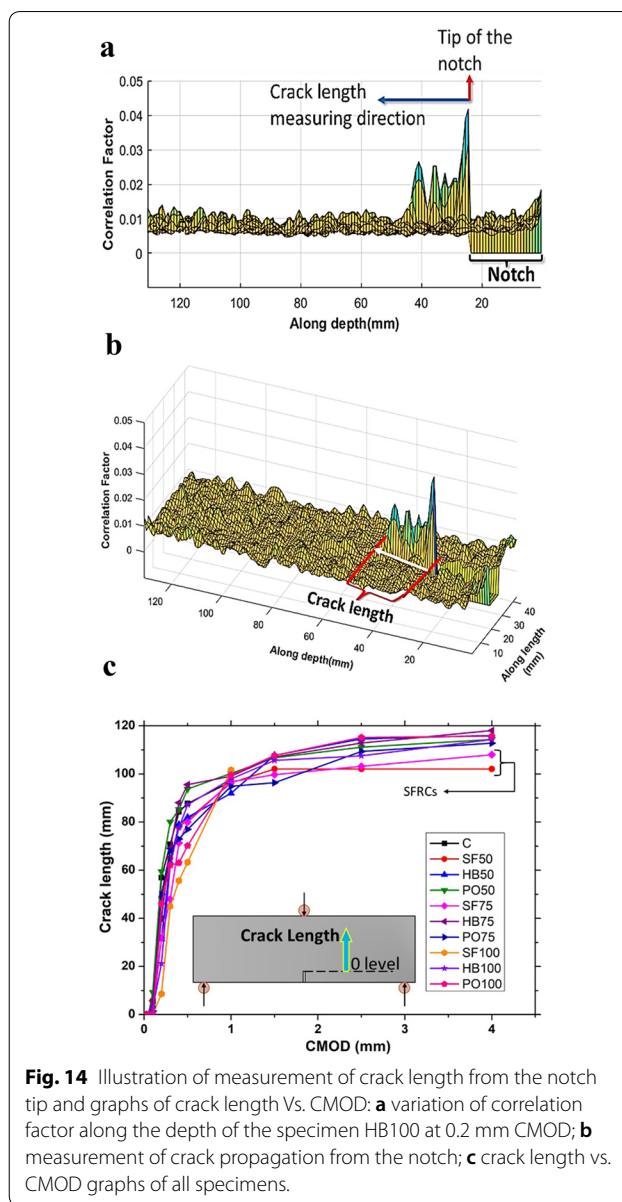
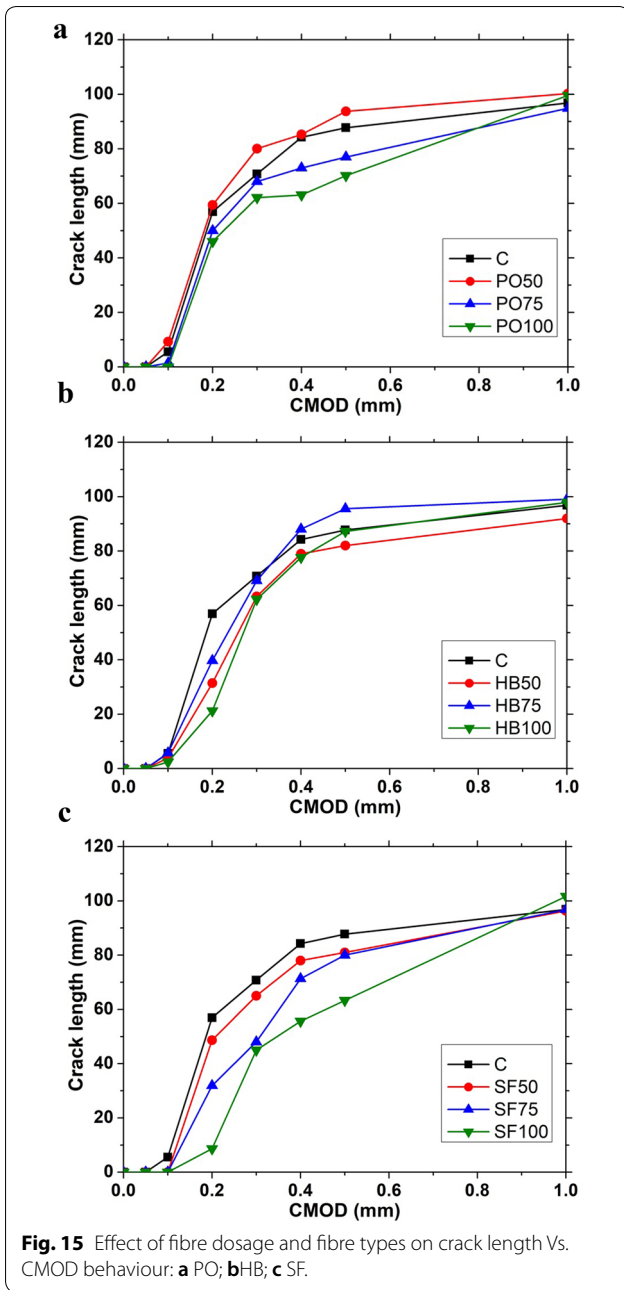


**Fig. 14** Illustration of measurement of crack length from the notch tip and graphs of crack length vs. CMOD: **a** variation of correlation factor along the depth of the specimen HB100 at 0.2 mm CMOD; **b** measurement of crack propagation from the notch; **c** crack length vs. CMOD graphs of all specimens.

was observed in the softening part of the load response immediately after the peak load (i.e. after nearly 0.05 mm CMOD), attributing to the hinge formation. To study this vital range of CMOD, Fig. 15 represents crack length versus CMOD graphs focusing on small CMOD values.

As indicated in Fig. 14, SFRC graphs were found in the bottom-most region designating that SFRC facilitated least crack lengths among all the FRCs. Steel fibres arrested the early opening of the crack effectively as well (Fig. 15). This indicates that for the same CMOD value, the crack length propagation from the notch has decreased due to the addition of stiff steel fibres, whereas SynFRC and HFRC specimens exhibited nearly similar



behaviour as that of the control specimen (Fig. 14). The graph in Fig. 14 is a representation of two phases in the crack propagation. The first zone is from 0 mm to 1 mm CMOD attributing to the hinge formation, where crack tip rapidly propagates through the section. The second zone is from 1 mm to 4 mm of CMOD attributing to the opening of the hinge, where the crack tip does not travel much vertically because of the crack bridging by the fibres. Figure 15 represents the comparison of crack length Vs. CMOD of different fibre types in the

hinge formation zone of up to a CMOD value of 1 mm. Although HFRC seems to have the lesser crack length for very small CMOD values (<0.3 mm), no significant difference was observed at higher CMOD values. However, it can be observed that the main contribution of fibres was to assist in the hinge formation (as shown in Figs. 9, 10, 11) and reduce the crack opening width during bending loads. All the fibre-reinforced specimens had much higher CMOD values compared to the control specimen. FRC specimens had better post-peak resistance due to the fibres bridging the crack and resisted the opening of the hinge.

The crack opening displacement (COD) as a function of the depth of the beam for different fibre types and fibre dosages is shown in Fig. 16. Different CMOD values (LP1 to LP5) are chosen for this comparison. The comparison shows that the COD at a particular height reduces with increase in fibre dosage. Similarly, COD values are lower at a particular height for steel fibres when compared to synthetic and hybrid fibre types. Using the contour of horizontal displacement ( $U_C$ ) (Fig. 13a and b), the variation of the crack opening displacement (COD) across the depth of the beam can be studied. The graphs thus obtained are represented in Fig. 16. These CODs represented are the jumps in  $U_C$  contours along with the depth of the beam above notch at each interval of 5 pixels. The tip of the notch was considered at zero levels. From Fig. 16, it can be observed that at all the loading points for different types of fibres, SynFRC and HFRC exhibit more or less similar COD distribution along the depth. However, the COD values are comparatively lesser at the same depths in SFRC. This states that SFRC facilitates minimum COD at the same LP arresting the crack in best fashion among the three. The control specimen ruptured completely. Also, the correlation for SF100 specimen broke down at about 1 mm CMOD corresponding to LP3. The hinging effect is also observed from these graphs in Fig. 16 for all specimens as the crack opening occurred around a hinge point at about 120 mm height from the notch.

### 5 Effect of Fibres on Fracture Process Zone (FPZ)

The cohesive stress distribution in the fracture process zone (FPZ) depends upon the stress-crack opening behaviour. Further, the stress-crack opening response depends upon the type of concrete and its composition. The characteristics of FPZ in plain concrete with no fibres and FRC can be very different. Previous studies have shown that micro-cracking in concrete occurs over a relatively large FPZ. The size of FPZ in small scale laboratory specimens can be of the same order of magnitude of the specimen itself. Thus, accurate estimation of FPZ should include testing of different sizes of

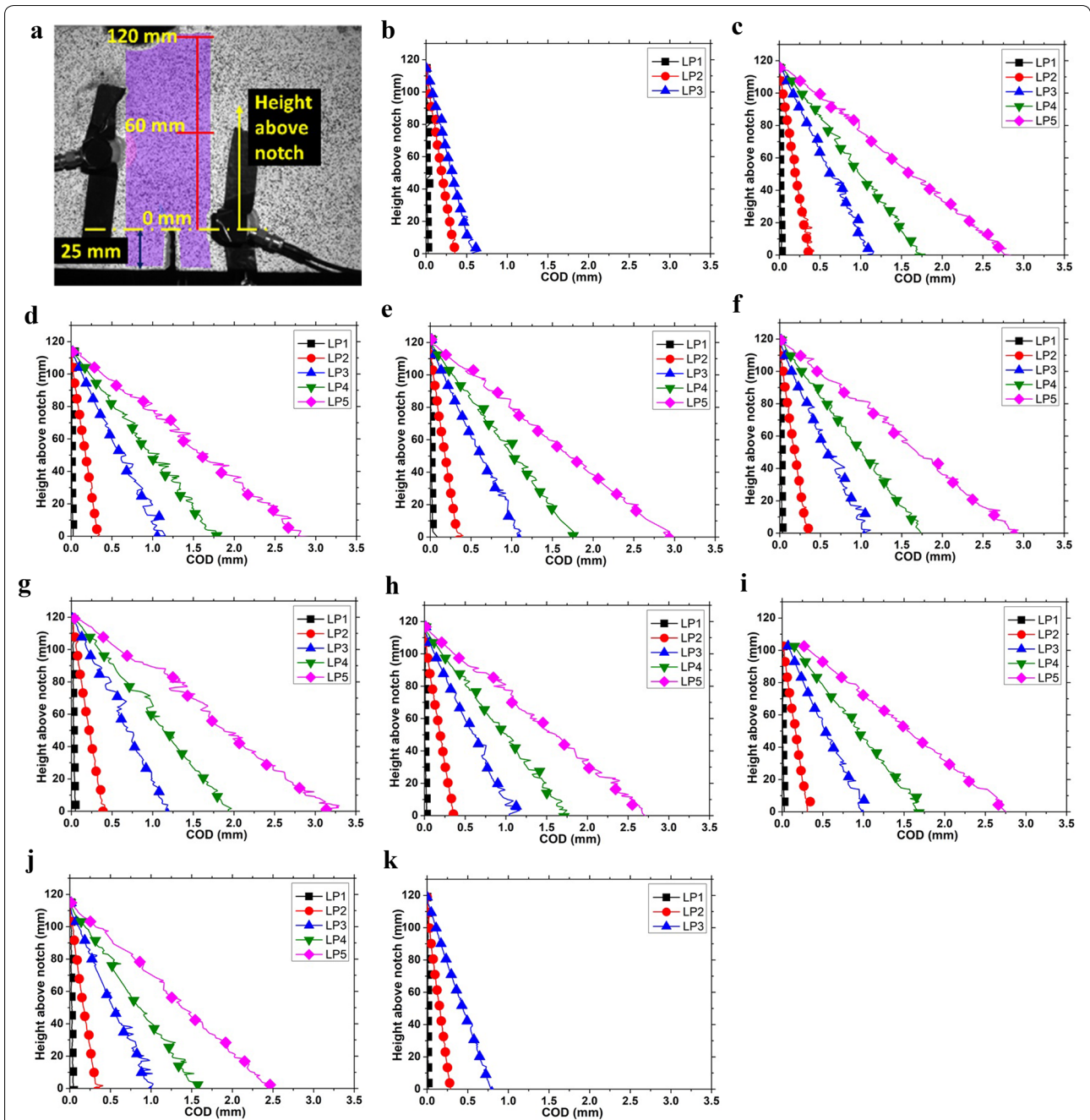


**Fig. 16** Distribution of COD along the depth for different fibre types and dosages at all loading points: **a** COD measurement from DIC; **b** control beam; **c** PO50; **d** PO75; **e** PO100; **f** HB50; **g** HB75; **h** HB100; **i** SF50; **j** SF75; **k** SF100 beams.

specimens to account for the size effect (Ha et al. 2015). For the measurement of FPZ length, identification of FPZ tip is necessary. The maximum tensile strain that concrete can withstand without forming a continuous crack is called the tensile strain capacity. Thus, the tip of FPZ for plain concrete with no fibres is defined as the location where the maximum tensile strain is reached. Maximum

tensile strain capacity of plain concrete is 150 micro-strain determined by experiment in this study. For the control specimens, the critical crack opening is calculated based on fracture energy as 0.147 N/mm and tensile strength of the concrete is 6 MPa (Wu et al. 2011). Thus, the critical crack opening ( $w_{0c}$ ) for the control beam with no fibres is calculated as 0.1 mm based on Eq. 8. If the

CTOD is smaller than  $w_{oc}$ , the FPZ is assumed to be not fully developed. The crack opening displacement is linearly proportional to the distance to the FPZ tip. At different loading points, the FPZ length can be measured by comparing the measured CTOD and the calculated value of  $w_{oc}$ :

$$w_{oc} = \frac{3.5G_f}{f_t} \tag{8}$$

In FRC, the stress–crack width relations depend upon fibre type and volume fractions. The traction free zone is assumed to occur after CMOD values of 3.5 mm. RILEM (Vandewalle et al. 2003) code defines an ultimate limit state of 3.5 mm of CMOD values after which the role of fibre in crack bridging is considered to be very minimum. The width of FPZ is fixed for control beam at the critical crack width of 0.1 mm as per previous investigations (Wu et al. 2011). The FPZ length is measured at different load points (LP) as shown in Fig. 8a. The respective image numbers are selected for all load points and grid data are extracted from VIC-2D™ analysed images for measurement of FPZ length. By using a MATLAB code, the tip of the FPZ (2-2) is identified, as shown in Fig. 17a. The tip of FPZ corresponds to the depth at which the strain in concrete reaches 150 micro-strain. The fracture process zone in plain concrete includes the micro-cracking, aggregate interlock and crack branching, as shown in Fig. 1a. In the case of FRC specimens, the FPZ length includes the micro-cracking, aggregate interlock, crack branching and fibre-bridging zone, as shown in Fig. 1b. The FPZ opening is considered as the traction free end, in which the cohesive stress is considered to be negligible. Thus, in the case of FRC specimens, the traction free zone is assumed to start when the crack opening displacement exceeds the critical crack width of 3.5 mm. However, the critical opening may change according to aggregate and fibre types. Understanding the effect of aggregate and fibre type on critical opening is scope for future work.

To understand the variation of the FPZ length for different fibre dosages, the change in FPZ length with respect to the crack length (notch depth plus crack extension length) at different loading points is plotted in Fig. 18. The length of FPZ increased significantly due to fibre addition. However, the role of fibre dosage and fibre type seems to be marginal. The FPZ length of control beam increased until its full development and decreased after that. It increased linearly to 42.7 mm up to peak load (Fig. 18). After that, the FPZ length of plain concrete specimen slowly reduced to 38 mm up to a crack length of 135 mm. Later, it significantly reduced to 21.5 mm as shown in Fig. 18. However, due to fibre addition, the FPZ length increased significantly for all fibre types. The FPZ length in all FRC specimens with PO, HB and

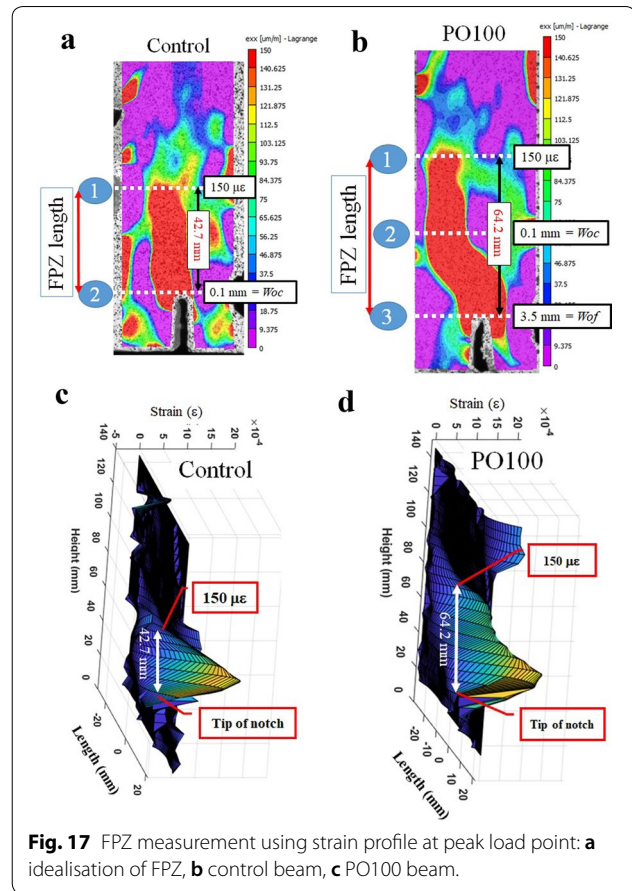


Fig. 17 FPZ measurement using strain profile at peak load point: a idealisation of FPZ, b control beam, c PO100 beam.

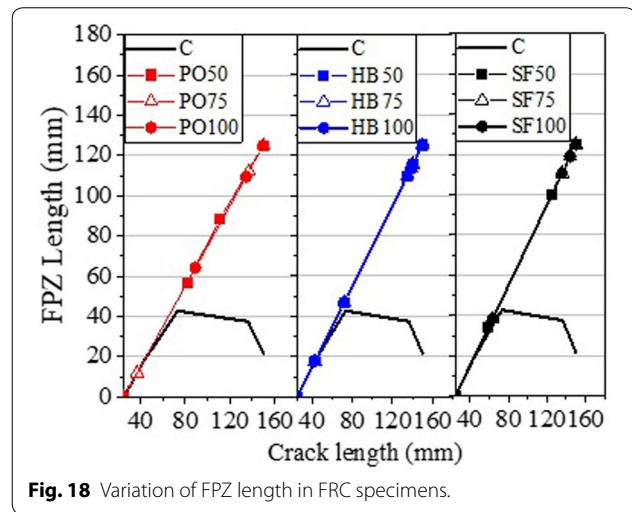


Fig. 18 Variation of FPZ length in FRC specimens.

SF fibres increased linearly up to 130 mm, as shown in Fig. 18. A linear variation of FPZ length with crack length was observed for all the fibre volume fractions and fibre types. No appreciable change in variation of FPZ length was observed due to the change in fibre dosage and fibre

types. Thus, in FRC specimens FPZ length was not fully developed leading to no traction free crack. This could be due to reduced ligament lengths available in the small size specimens considered in this study. Previous studies have shown that fracture energy, process zone length and brittleness of concrete depends on the size effect (Wu et al. 2011, Dai et al. 2019). FPZ is not only a material property and is greatly influenced by the specimen size (Ha et al. 2015). Thus, for an accurate understanding of the evolution of FPZ in FRC, further research is required.

## 6 Scope for Further Work

Only limited specimens were tested as part of this study to understand the effect fibres and their combinations on fracture behaviour. Thus, for an accurate understanding of the evolution of FPZ in FRC, more research is further required. In particular, the following aspects need to be studied in detail:

1. The effect of different fibre types and their combinations on the fracture behaviour of specimens of different sizes.
2. Effect of initial notch size and the ratio of notch length to the height of the specimen on the fracture behaviour of FRC.
3. The fracture characteristics of specimens with different sizes and fibre types can be effectively studied by the simultaneous application of DIC and acoustic emission techniques. By this, the evolution of the length and width of FPZ and crack openings in scaled FRC specimens using the DIC technique can be correlated with the results obtained from acoustic emission.

## 7 Summary and Conclusions

FRC beams reinforced with different combinations of synthetic and steel fibres were tested under bending to investigate the fracture behaviour. The effect of fibre dosage and their types of fracture behaviour was evaluated using DIC analysis. Variation in post-cracking behaviour and crack-width openings with respect to crack tip opening was studied for evaluating the fracture performances of different FRC. The following conclusions can be drawn from the limited results presented in this study:

1. Mixing of two different fibres of dissimilar physical and mechanical properties in HFRC exhibited synergy by showing good performance over a wide range of CMODs, unlike the individual ones which performed well in their specific ranges of CMODs.
2. The difference between the minimum ( $F_{\min}$ ) and maximum post-cracking load resistance ( $F_{\max}$ )

increased with an increase in fibre dosage for all the types of fibres. However, the difference between peak load ( $F_L$ ) and the maximum post-cracking load ( $F_{\max}$ ) resistance decreased with an increase in fibre dosage.

3. The improvement in toughness of FRC specimens due to the addition of PO, HB and SF fibres, respectively, ranges from 3 to 8, 6 to 10 and 8 to 14 times to that of the control specimens.
4. The comparison of flexural strengths at the initial crack openings of SynFRC indicates its disadvantage with the least flexural strengths among all the fibre types used in this study.
5. For the same fibre type, the crack length decreases significantly with an increase in the volume fraction of fibre for a given CMOD. The crack length of SFRC was smaller than a hybrid and synthetic ones for a given CMOD. Due to better crack arresting, significant improvements in the post-cracking load resistance response can be observed in SFRC specimens.
6. Fibre volume dosages play a vital role in the enhancement of the rate of load recovery after cracking. Increase in volume fraction significantly increases the maximum post-peak load resistance in all types of fibres considered in this study.
7. Fracture process zone length increased significantly due to fibre addition. However, the influence of fibre dosage and fibre types on FPZ seems to be negligible for the size of the specimen considered in this study. More research should focus on the size effect and notch characteristics on understanding the role of fibres in fracture behaviour.

### Authors' information

ABB is a graduate student at IIT Hyderabad. SSP is an Associate Professor at IIT Hyderabad.

### Acknowledgements

Not applicable.

### Authors' Contributions

ABB was a significant contributor to performing the tests and writing the manuscript. SSP analysed the data and provided inputs to the analysis and interpretation of results. Both authors read and approved the final manuscript.

### Funding

The authors would like to thank the UAY project (Sanction # UAY-2016-IITH\_008) for partially funding this research project.

### Availability of Data and Materials

The datasets used and/or analysed during the current study are available from the corresponding author on reasonable request.

### Competing Interests

The authors declare that they have no competing interests.

Received: 17 September 2019 Accepted: 5 August 2020  
Published online: 28 September 2020

## References

- Aggelis, D. G., Soulioti, D., Barkoula, N. M., Paipetis, A. S., Matikas, T. E., & Shotani, T. (2010). Acoustic emission monitoring of steel fiber reinforced concrete under bending. *Journal of Acoustic Emission*, 28, 32–40.
- Alam, S. Y., Saliba, J., Loukili, A., 2012. Study of evolution of fracture process zone in concrete by simultaneous application of digital image correlation and acoustic emission. VIII Int. Conf. Fract. Mech. Concr. Concr. Struct. 1–9.
- Alam, S. Y., Saliba, J., & Loukili, A. (2014). Fracture examination in concrete through combined digital image correlation and acoustic emission techniques. *Construction and Building Materials*, 69, 232–242. <https://doi.org/10.1016/j.conbuildmat.2014.07.044>.
- Alberti, M., Enfedaque, A., & Gálvez, J. (2015). Improving the reinforcement of polyolefin fiber reinforced concrete for infrastructure applications. *Fibers*, 3, 504–522. <https://doi.org/10.3390/fib3040504>.
- Alhozaimy, A. M., Soroushian, P., & Mirza, F. (1996). Mechanical Properties of Polypropylene Fiber Reinforced Concrete and the Effects of Pozzolanic Materials. *Cem. Concr. Compos.*, 9465, 85–92.
- Banthia, N., & Sappakittipakorn, M. (2007). Toughness enhancement in steel fiber reinforced concrete through fiber hybridisation. *Cement and Concrete Research*, 37, 1366–1372. <https://doi.org/10.1016/j.cemconres.2007.05.005>.
- Bhosale, A., Rasheed, M. A., Prakash, S. S., & Raju, G. (2019). A study on the efficiency of steel vs. synthetic vs. hybrid fibers on fracture behavior of concrete in flexure using acoustic emission. *Construction and Building Materials*, 199, 256–268. <https://doi.org/10.1016/j.conbuildmat.2018.12.011>.
- Bhowmik, S., & Ray, S. (2019). An experimental approach for characterisation of fracture process zone in concrete. *Engineering Fracture Mechanics*, 211, 401–419. <https://doi.org/10.1016/j.engfracmech.2019.02.026>.
- BS EN 14651, 2005. Test method for metallic fibred concrete — Measuring the flexural tensile strength (limit of proportionality (LOP), residual). Br. Stand. Inst. 3, 1–17.
- Buratti, N., Mazzotti, C., & Savoia, M. (2011). Post-cracking behaviour of steel and macro-synthetic fibre-reinforced concretes. *Construction and Building Materials*, 25, 2713–2722. <https://doi.org/10.1016/j.conbuildmat.2010.12.022>.
- Caggiano, A., Cremona, M., Faella, C., Lima, C., & Martinelli, E. (2012). Fracture behavior of concrete beams reinforced with mixed long/short steel fibers. *Construction and Building Materials*, 37, 832–840. <https://doi.org/10.1016/j.conbuildmat.2012.07.060>.
- Chiranjeevi Reddy, K., & Subramaniam, K. V. L. (2017). Experimental investigation of crack propagation and post-cracking behaviour in macrosynthetic fibre reinforced concrete. *Magazine of Concrete Research*, 69, 467–478. <https://doi.org/10.1680/jmacr.16.00396>.
- Crammond, G., Boyd, S. W., & Dulieu-barton, J. M. (2013). Speckle pattern quality assessment for digital image correlation. *Optics and Lasers in Engineering*, 51, 1368–1378. <https://doi.org/10.1016/j.optlaseng.2013.03.014>.
- Dai, S., Liu, X., & Nawnit, K. (2019). Experimental study on the fracture process zone characteristics in concrete utilising DIC and AE methods. *Applied Science*. <https://doi.org/10.3390/app9071346>.
- Deng, Z., & Li, J. (2007). Mechanical behaviors of concrete combined with steel and synthetic macro-fibers. *Comput Concr*, 4, 207–220. <https://doi.org/10.12989/cac.2007.4.3.207>.
- Eurocode (EN14889-2), (2007). *EN 14889-2, Fibers for concrete, polymer fibers, definitions, specification and conformity*. Belgium: Bruxelles.
- Gali, S., & Subramaniam, K. V. L. (2017). Evaluation of crack propagation and post-cracking hinge-type behavior in the flexural response of steel fiber reinforced concrete. *International Journal Concrete Structure Materials*, 11, 365–375. <https://doi.org/10.1007/s40069-017-0197-4>.
- Ha, K., Baek, H., & Park, K. (2015). Convergence of fracture process zone size in cohesive zone modeling. *Applied Mathematical Modelling*, 39, 5828–5836. <https://doi.org/10.1016/j.apm.2015.03.030>.
- Hu, Z., Xie, H., Lu, J., Wang, H., & Zhu, J. (2011). Error evaluation technique for three-dimensional digital image correlation. *Applied Optics*, 50, 6239–6247. <https://doi.org/10.1364/AO.50.006239>.
- IS 10262: 2009, 2009. Indian concrete mix design guide lines.
- Lakavath, C., Bhosale, A., Prakash, S. S., 2020. Experimental Investigation on Crack-Arresting Mechanism of Steel Fibre-Reinforced Concrete Prism Specimens Using DIC and AE Techniques. [https://doi.org/10.1007/978-981-15-4079-0\\_5](https://doi.org/10.1007/978-981-15-4079-0_5)
- Lakavath, C., Joshi, S. S., & Prakash, S. S. (2019). Investigation of the effect of steel fibers on the shear crack-opening and crack-slip behavior of prestressed concrete beams using digital image correlation. *Engineering Structures*, 193, 28–42. <https://doi.org/10.1016/j.engstruct.2019.05.030>.
- Lecomptea, D., Smitsb, A., Bossuytb, S., Solb, H., Vantommea, J., Van Hemelrijckb, D., et al. (2005). Quality assessment of speckle patterns for digital image correlation. *Optics and Lasers in Engineering*, 44, 1132–1145. <https://doi.org/10.1016/j.optlaseng.2016.11.001>.
- Li, B., Xu, L., Shi, Y., Chi, Y., Liu, Q., & Li, C. (2018). Effects of fiber type, volume fraction and aspect ratio on the flexural and acoustic emission behaviors of steel fiber reinforced concrete. *Construction and Building Materials*, 181, 474–486. <https://doi.org/10.1016/j.conbuildmat.2018.06.065>.
- Oh, B. H., Kim, J. C., & Choi, Y. C. (2007). Fracture behavior of concrete members reinforced with structural synthetic fibers. *Engineering Fracture Mechanics*, 74, 243–257. <https://doi.org/10.1016/j.engfracmech.2006.01.032>.
- Park, J., Yoon, S., Kwon, T., & Park, K. (2017). crossmark. *Optics and Lasers in Engineering*, 91, 62–72. <https://doi.org/10.1016/j.optlaseng.2016.11.001>.
- Rasheed, M. A., & Prakash, S. S. (2015). Mechanical behavior of sustainable hybrid-synthetic fiber reinforced cellular light weight concrete for structural applications of masonry. *Construction and Building Materials*, 98, 631–640. <https://doi.org/10.1016/j.conbuildmat.2015.08.137>.
- Rasheed, M. A., & Prakash, S. S. (2018a). Experimental study on compression behavior of fiber-reinforced cellular concrete stack-bonded masonry prisms. *ACI Materials Journal*, 115, 149–160. <https://doi.org/10.14359/51701241>.
- Rasheed, M. A., & Prakash, S. S. (2018b). Behavior of hybrid-synthetic fiber reinforced cellular lightweight concrete under uniaxial tension – Experimental and analytical studies. *Construction and Building Materials*, 162, 857–870. <https://doi.org/10.1016/j.conbuildmat.2017.12.095>.
- Reu, P. (2015). All about speckles: Speckle density. *Exp. Tech.*, 39, 1–2. <https://doi.org/10.1111/ext.12161>.
- Robins, P., Austin, S., Chandler, J., & Jones, P. (2001). Flexural strain and crack width measurement of steel-fibre-reinforced concrete by optical grid and electrical gauge methods. *Cement and Concrete Research*, 31, 719–729. [https://doi.org/10.1016/S0008-8846\(01\)00465-3](https://doi.org/10.1016/S0008-8846(01)00465-3).
- Sahoo, S. S., Kumar, A. S., & Prakash, S. S. (2020). Mechanical characterisation of structural lightweight aggregate concrete made with sintered fly ash aggregates and synthetic fibres. *Cement Concrete Composition*, 113, 103712. <https://doi.org/10.1016/j.cemconcomp.2020.103712>.
- Skarzynski, L., & Tejchman, J. (2013). Experimental investigations of fracture process using DIC in plain and reinforced concrete beams under bending. *Strain*, 49, 521–543. <https://doi.org/10.1111/str.12064>.
- Srikar, G., Anand, G., & Prakash, S. S. (2016). A study on residual compression behavior of structural fiber reinforced concrete exposed to moderate temperature using digital image correlation. *International Journal of Concrete Structures and Materials*, 10, 75–85. <https://doi.org/10.1007/s40069-016-0127-x>.
- Sutton, M., Orteu, J., Schreier, H., 2009. *Image correlation for shape, motion and deformation measurements*, Springer, New York, doi: <https://doi.org/10.1007/978-0-387-78747-3>
- UNI 11039-2:2003, 2003. Steel fibre reinforced concrete – test method for determination of first crack strength and ductility indexes.
- Vandewalle, L., Nemegeer, D.B., Balazs, L., Hungary; B. Barr, UK; J. Barros, Portugal; P. Bartos, UK; N. Banthia, Canada; M. Criswell, USA; E. Denarié, Suisse; M. Di Prisco, Italy; H. Falkner, Germany; R. Gettu, Spain; V. the N., 2003. RILEM TC 162-TDF: ‘Test and design methods for steel fibre reinforced concrete’. *Rilem Tc 162-Tdf* 36, 560–567.
- Wu, Z. M., Rong, H., Zheng, J. J., Xu, F., & Dong, W. (2011). An experimental investigation on the FPZ properties in concrete using digital image correlation technique. *Engineering Fracture Mechanics*, 78, 2978–2990. <https://doi.org/10.1016/j.engfracmech.2011.08.016>.
- Yang, R. C. (2014). A regularised finite-element digital image correlation for irregular displacement field. *Optics and Lasers in Engineering*, 56, 67–73. <https://doi.org/10.1016/j.optlaseng.2013.12.013>.

## Publisher's Note

Springer Nature remains neutral with regard to jurisdictional claims in published maps and institutional affiliations.